RF-Mediator: Tuning Medium Interfaces with Flexible Metasurfaces

Ruichun Ma
ruichun.ma@yale.edu

Wenjun Hu
wenjun.hu@yale.edu

ABSTRACT

Emerging wireless IoT applications increasingly venture beyond over-the-air communication, such as deep-tissue networking for medical sensors, air-water communication for oceanography, and soil sensing for agriculture. These applications face the fundamental challenge of significant reflection and power loss at medium interfaces. We present RF-Mediator, a programmable metasurface placed near a medium interface to mask the presence of a physical boundary. Our hardware design comprises a single layer of varactor-based surface elements with specific metallic patterns and wiring. With the biasing voltage tuned element-wise, the surface dynamically mediates between the adjacent media to minimize unwanted reflection and boost transmission through the medium interface. A multi-stage control algorithm efficiently determines the surface configuration to handle all dynamic adaptation needs for medium impedance matching and beamforming jointly. We implement a lightweight and flexible metasurface prototype and experiment with diverse cross-medium setups. Extensive evaluation shows that RF-Mediator provides a median power gain of 8 dB for air-tissue links and up to 30 dB for cross-medium backscatter links.

CCS CONCEPTS

• **Hardware** → **Wireless devices**; • **Networks** → **Wired access networks**.

KEYWORDS

Cross-Medium, Wireless, Metasurfaces, Impedance Matching, Beamforming

1 INTRODUCTION

New wireless Internet of Things (IoT) applications increasingly involve communication media not limited to air only. The signals may need to cross over medium boundaries, especially air-tissue interfaces [12, 28, 35, 42, 59, 66], air-water interfaces [22, 56], and air-ground interfaces [25, 37]. Air-tissue networking is the key enabler for numerous *in-vivo* medical applications, such as vital sign monitoring [20, 57], wireless gastrointestinal diagnosis [43, 52], on-demand drug delivery [38], and untethered neuro-stimulation therapy [51, 53]. Air-water networking arises in the course of marine biological sensing, underwater IoT, monitoring submerged sites [11]. Air-ground networking is useful for underground operations [15, 50] and soil sensing applications [25, 36].

Cross-medium networking, however, is much more challenging than its over-the-air counterpart (Section 2). When two adjacent media exhibit different propagation characteristics, some signal power is reflected back by the medium interface rather than crossing the interface (Figure 1). Such reflection can be substantial, e.g., around 90% of the signal power is reflected for air-to-tissue links on 2.4 GHz (Figure 2), reducing the through-interface signal power by 10 dB and creating strong, unwanted reflections. This happens in both directions, i.e., whether air-to-tissue or tissue-to-air, which is especially significant for backscatter devices with low transmission power to start with. Strong reflections can further cause severe self-interference and multipath fading.

Most existing solutions operate at the communication endpoints, boosting the transmitted or received power via some form of beamforming [28, 42, 59] or moving the endpoints to the interface [13, 17, 18]. While these *compensate for* the power loss at the interface or *avoid* crossing the interface, they cannot address the root cause of the cross-medium challenge, thus leading to side effects (Section 2.2).

Fundamentally, medium permittivity differences cause impedance mismatch at the interface (Section 2.1). If we consider propagation media as transmission lines for signals, conceptually, we can place an RF component at the medium interface for matching. This is a perspective shift from conventional impedance control [32], targeting dynamic environments instead of highly controlled circuit boards.

A smart surface is well suited to the role of impedance matching between media, the simplest of which is an array of antenna-like elements or patterns acting as a *non-programmable surface*. There has been significant interest in

(a) Without RF-Mediator   **(b)** With RF-Mediator
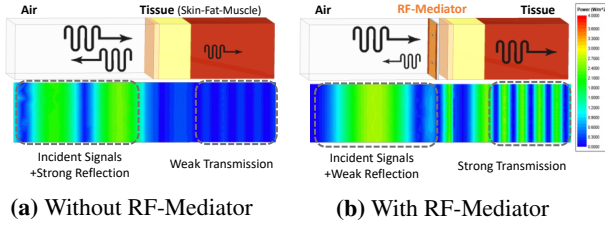
Figure 1: RF-Mediator matches the impedance of adjacent media for wave propagation (left-to-right). The heat maps show signal power distributions.
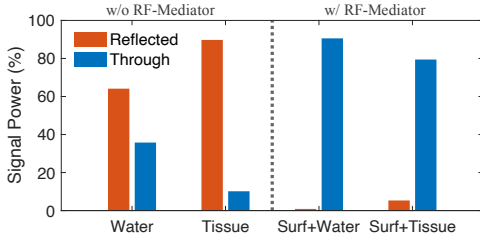
Figure 2: Reflected and transmitted-through power at air-water and air-tissue interfaces. RF-Mediator minimizes reflection and boosts through-interface transmission.

augmenting or programming the radio propagation environment with smart surfaces (e.g., [14, 23, 24, 27, 29, 39, 41, 45, 60, 67, 68]) by controlling the signal propagation behavior and improve the endpoint-perceived channel conditions. However, these designs for over-the-air propagation cannot alter the unfavorable propagation behavior when crossing a medium interface. Further, their beamforming capability may degrade due to coupling with a close-by non-air medium. Recent proposals have made headway designing multi-layer metasurfaces for cross-medium reflection mitigation [64, 65]. However, these are one-off, *non-programmable* hardware designs far from handling real-world medium dynamics and wireless channel fluctuations. Further, these designs forego the beamforming gain in previous endpoint-centric solutions, which can be significant in our experiments. Practically, thick, rigid circuit boards are ill-suited for deployment.

Instead, we present RF-Mediator, a single-layer *programmable* metasurface to be placed *near* the medium interface (Section 3). It masks the presence of the physical media boundary, such that two (or more) media appear to be a single medium virtually, by dynamically mediating the impedance of adjacent media to boost transmission through the boundary. Figure 1 shows the signal power distributions at an air-tissue interface. With RF-Mediator, most power traverses the interface and little is reflected back to air.

The design for RF-Mediator addresses several challenges. First, we need a hardware design that can achieve dynamic medium impedance matching and beamforming. Our surface hardware comprises carefully designed metallic patterns, interconnected with varactor diodes, and individually controlled

biasing voltage wires. Adjusting the varactor biasing voltages produces a tunable surface admittance range specific for our medium impedance matching purposes; The element-wise on-off control effect achieves an additional beamforming gain (Section 3.3). Second, we need an efficient control algorithm for impedance matching while adapting to environmental dynamics, such as different medium compositions, varying surface-medium gaps, and fluctuating multipath channel conditions. In particular, the effects of impedance matching and beamforming cannot be completely decoupled. Our multi-stage algorithm caters to all needs at once, by successively performing surface-wide coarse-grained impedance matching, element-wise beamforming, then fine-grained voltage adjustment jointly optimizing both functionalities (Section 3.4). Third, practically, the surface needs to be lightweight and adaptable to medium interface shapes across diverse application scenarios. Our low-complexity design allows implementation as flexible and conformal prototypes.

We fabricated RF-Mediator prototypes on a thin, flexible PCB substrate (Section 4, Figure 10). For air-tissue networking, the surfaces can be incorporated in garments like blankets or hospital gowns for medical purposes [52]. For air-water networking, the surfaces can mimic floating aquatic plant leaves, bridging on-land gateways and underwater IoT devices. For air-soil networking, the surfaces may take the form of agricultural mulch films, assisting drones with data collection from underground sensors [58].

Extensive evaluation (Section 5) shows we reduce the reflection at air-water and air-tissue interfaces by over 10 dB, confirming adequate medium impedance matching. We achieve a median throughput increase of 55% and up to 4× for air-water Wi-Fi links. For (emulated) in-water backscatter links, our system provides a median received power gain of 10 dB and up to 30 dB. RF-Mediator's programmability lends to robust performance despite medium consistency variation (tissue fat thickness), surface-medium gaps, varying channel conditions, and surface-endpoint distances.

In summary, this paper makes the following contributions. First, we highlight a new signal manipulation modality, i.e., dynamic impedance matching of adjacent media, and identify the knobs for programmability to support cross-medium wireless networking. We also show the importance of further incorporating beamforming. Second, we propose the first electronically programmable impedance-matching metasurface design. Together with an efficient, multi-stage control algorithm, our design constitutes an end-to-end system that dynamically controls signal propagation (reflection and transmission) and beamforming jointly at medium interfaces. Third, we present a lightweight and flexible metasurface implementation that facilitates practical deployment. Experiments confirm that we can effectively mask the presence of a physical media boundary with RF-Mediator.

2 BACKGROUND AND MOTIVATION

We first explain RF signal propagation behavior across any medium interface. Then we summarize existing cross-medium solutions and their shortcomings to motivate our design.

2.1 Signal Propagation at Medium Interfaces

Transmission and reflection. We characterize a medium with two parameters: *relative permittivity* ϵ_r and *relative permeability* μ_r, which describe wave propagation relative to vacuum. The intrinsic wave impedance of the medium, denoted as $Z = \frac{\sqrt{\mu_r}}{\sqrt{\epsilon_r}} Z_0$ (with $Z_0 = 376.7\Omega$ representing the vacuum impedance), captures the electric-to-magnetic field strength ratio [49]. Given that μ_r is unitary for typical media of interest, the medium impedance is primarily governed by the *permittivity*, ϵ_r.

Suppose signals travel from air (relative permittivity $\epsilon_0 = 1$, impedance Z_0) to another medium of interest (ϵ_r, Z_r). Solving the boundary conditions at the interface [49] gives

$$\Gamma = \frac{Z_r - Z_0}{Z_r + Z_0} = \frac{\sqrt{\epsilon_0} - \sqrt{\epsilon_r}}{\sqrt{\epsilon_0} + \sqrt{\epsilon_r}}$$
$$T = 1 + \Gamma = \frac{2Z_r}{Z_r + Z_0} = \frac{2\sqrt{\epsilon_0}}{\sqrt{\epsilon_0} + \sqrt{\epsilon_r}} \qquad (1)$$

where Γ and T are the reflection and transmission coefficients of the interface respectively. When the impedance values of adjacent media are not equal or matched, some signal power is reflected at the interface instead of propagating to the other medium. The through-interface power is $\frac{Z_0}{Z_r}|T|^2$, while the power reflected from the interface is $|\Gamma|^2$. Such power loss at the interface happens in both propagation directions.

Table 1 lists the parameters of several media measured in controlled lab settings [30, 44, 64], and Figure 2 shows the propagation behavior through medium pairs simulated with these parameters in HFSS. Notably, water and tissue (skin, fat, muscle) exhibit higher permittivity, resulting in pronounced reflection and weak transmission at air-water and air-tissue interfaces. Tissue comprises several layers, including skin, fat, and muscle, non-uniform in thickness, leading to multiple reflections before signals reach an in-vivo endpoint. While the exact permittivity values vary slightly in practice depending on the specific medium composition and measurement method, the overall propagation behavior remains the same.

Attenuation and refraction. Common media, like tissue and water, can have high *conductivity*, adding an imaginary part to make permittivity complex-valued and causing notable signal attenuation. For the media considered in this paper, however, their conductivity values are within the range that does not affect the medium impedance significantly. Another phenomenon at the medium interface is signal refraction, which changes the propagation direction. This contributes to multipath fading of through-interface signals. Attenuation

Table 1: Intrinsic impedance of medium, determined by permittivity, causes impedance mismatch between media.

Medium	Air	Water	Skin	Fat	Muscle
Permittivity	1	81	43.75	5.46	55.03
Impedance (Ω)	376.7	41.86	57.0	161.2	50.8

and refraction weaken through-interface signal power but do not affect medium impedance (mis)match.

Backscatter signals. Backscatter signals, pivotal for battery-less in-vivo communication [12, 28, 35, 42, 59, 66], encounter amplified challenges at medium interfaces due to the signals propagating through these interfaces twice—once outbound and once inbound. For example, air-tissue backscatter links require the in-vivo endpoints to harvest enough power and the in-air endpoints to receive backscattered signals at sufficient SINR (signal-to-interference-plus-noise ratio). The former is susceptible to the significant through-interface power loss already discussed. For the latter, the received backscatter signals incur reflection power loss twice, in both directions through the medium boundary. Further, strong reflections at the interface also create *self*-interference, significantly decreasing the received SINR at either endpoint.

Combined effects. Collectively, the propagation mechanisms produce three effects: *strong reflection-induced interference*, *through-interface power loss*, and *more complex multipath fading* inside the second medium. Ideally, solutions for cross-medium link improvement should counter all three issues.

2.2 Existing solutions and our approach

Enhancing in-vivo endpoints. One common strategy is to *compensate for through-interface power degradation after the fact* via receiver-side beamforming [28, 42] or more effective in-vivo receiver design [12, 59]. However, after-the-fact compensation is usually not as effective as tackling the root cause. It fails to counter the strong reflection at interfaces, causing power waste and large (self-)interference to nearby endpoints. It is also costly, requiring specialized and synchronized multi-antenna hardware or complex receiver design.

Placing endpoints at the interface. Alternatively, some endpoints can be moved to the medium interface instead to *avoid traversing an interface*, at the expense of limited usability. For example, specially designed antennas [13, 17, 18] on the skin bring discomfort and inhibit mobility, thus hindering long-term monitoring. Deploying an (active) endpoint at the interface usually demands battery power and precludes reusing existing IoT devices as the signal source.

Adding anti-reflection metasurfaces. Unlike endpoint-based approaches, adding metasurfaces to the medium boundary can fundamentally *minimize reflection*. Existing designs [21, 26, 31, 33, 64, 65], however, target a specific medium setup and cannot adapt or generalize to diverse scenarios. Nor do they
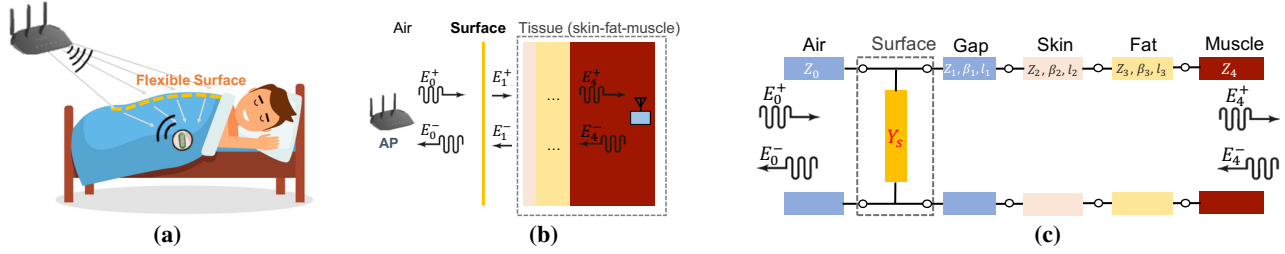
Figure 3: Surface operation illustration. (a) Air-to-tissue application example: An AP connects to an in-body (backscatter) endpoint through a metasurface for long-term medical monitoring. **(b)** Analytical model of the metasurface and tissue layers. **(c)** Microwave circuit model. We use a cascaded two-port (circles in the figure) microwave network to model signal propagation, deriving the desired *surface admittance (Y_s)* to minimize the reflection, E_0^-, and boost the through-interface transmission, E_4^+.

deal with multipath fading. They rely on multiple layers of thick and rigid dielectric substrate to host the metasurface, with a fixed placement with respect to the medium interface, both restricting practical deployment. Lastly, these efforts primarily focus on theoretical analysis, lacking end-to-end system design and experimental validation.

Non-RF signals. Other than RF signals, magnetic, acoustic, and light waves have also been explored, which involve various trade-offs in terms of range, datarate, power, hardware complexity, and availability. For example, magnetic inductive coupling and, more recently, magnetoelectric effect [66] boast of high power efficiency and small size, but supporting a shorter (2 cm) in-vivo link range than radiative approaches and requiring actively powered coils on the skin. Tarf [56] and AmphiLight [22] use acoustic and laser respectively for air-water links, but adopt application-specific approaches and require specialized endpoints.

Our approach. We present RF-Mediator, a flexible single-layer metasurface with programmable medium impedance matching and beamforming capability. By matching the impedance of adjacent media dynamically, we *address the root cause of unfavorable signal propagation bahavior* and mask the fact that signals traverse a physical medium boundary, allowing for air gaps and variable-thickness layers. We do not directly tackle signal attenuation or refraction, but account for these via the perceived channel conditions at the receiver and mitigate their effects with beamforming. Moreover, our single-layer design on a flexible substrate improves applicability in diverse scenarios.

Our approach is complementary and orthogonal to existing efforts improving *endpoints*, thus not directly comparable. RF-Mediator can work together with both purpose-built cross-medium endpoints and commodity IoT devices. Further, metasurfaces are low-power passive devices, enhancing through-surface power from external signal sources. Our lightweight design requires no direct contact between the metasurface and the medium interface, decoupling the relative placement of the two via surface programmability.

We focus on RF signals for their relatively long ranges, high datarates, hardware availability and significant interest in them [52, 55]. Conceptually, a metasurface can be added to the medium interface regardless of what signal, e.g., acoustic waves [19, 34, 40], but the specific surface design and the quantitative cost-benefit tradeoffs depend on the signal type.

3 RF-MEDIATOR DESIGN
We first outline the metasurface operational principle, along with a circuit model analysis to identify design requirements. We then describe the hardware design and an efficient multi-stage algorithm for surface configuration.

3.1 Operational Principle
Metasurfaces alter wave propagation via surface currents induced by incident waves, enforcing a specific electromagnetic boundary condition to allow different fields on both sides of the surface, as per Maxwell's equations [26, 48]. However, medium impedance matching does not happen solely on the metasurface but proceeds via intricate multi-order resonance between the metasurface and the medium/media. We examine wave propagation through a metasurface and an air-tissue interface (Figure 3(a)), to identify the knob for programmability and model diverse deployment scenarios.

Modeling signal propagation. Figure 3(b) shows the analytical model for RF signals traversing the metasurface and an air-tissue interface, where the tissue is a layered composition of skin, fat, and muscle. From the sender on the left, the signals propagate towards and through the surface, any potential gap, then the successive tissue layers. The gap between the surface and tissue, not fixed in thickness, may contain air, fabric, or other materials, embodying different deployment scenarios. This approach decouples the surface placement from the medium interface location to facilitate deployment. Upon reaching the tissue, the signals navigate through the body's layered composition towards the in-vivo receiver. The total electric field within each medium comprises the forward propagating waves, E^+, and the backward propagating E^- [49].

We want to minimize the reflection, E_0^-, from the interface and maximize the through-interface transmission, E_4^+.

Characterization as circuit components. We extend the basic medium boundary characterization (Section 2.1) to analyze the complex interplay between multi-layer medium composition and the metasurface. Waves resonate, i.e., bounce back and forth, between different layers and the surface and also experience various phase delays with respect to the medium segment thicknesses. We model such interactions explicitly, including effects of the surface-medium gap and complex medium composition, with a microwave circuit model shown in Figure 3(c). Each medium segment is viewed as a transmission line, characterized by its intrinsic impedance Z, phase constant β, and length l. As the metasurface operates via surface currents, we model the surface as a shunt circuit component with ***surface admittance*** $Y_s = G + jB$ [47, 64, 65]. The *admittance* describes how easily a circuit allows currents to flow, which comprises the *conductance G* (the real part) and the *susceptance B* (the imaginary part). The surface element design determines the precise value of surface admittance. Ideally, a lossless surface would have a minimal conductance, relying on the susceptance B for effective medium impedance matching. As the admittance increases, stronger surface currents are induced, causing more significant alterations on the amplitude and phase of propagating signals. We use admittance (the reciprocal of impedance) instead of impedance here to avoid handling an infinitely large impedance value.

Cascading all components. We analyze the circuit components above as a cascade of two-port microwave circuit networks (Figure 3(c), ports marked with circles). A 2×2 transmission matrix, i.e., the ABCD matrix, can characterize each circuit component. This matrix is defined by the relation between the total electric and magnetic field magnitudes at the two ports. Multiplying successive matrices can then easily capture the multi-order reflections and transmissions between the surface and multiple tissue layers.

For the whole cascaded circuit model, the matrix is

$$\begin{bmatrix} E_0 \\ H_0 \end{bmatrix} = \begin{bmatrix} A & B \\ C & D \end{bmatrix} \begin{bmatrix} E_4 \\ H_4 \end{bmatrix} \qquad (2)$$

We find the overall ABCD matrix by multiplying known matrices of the surface and tissue layers, which are a shunt circuit component and transmission lines [49].

$$\begin{bmatrix} A & B \\ C & D \end{bmatrix} = \begin{bmatrix} 1 & 0 \\ Y_s & 1 \end{bmatrix} \prod_{k=1}^{3} \begin{bmatrix} \cos \beta_k l_k & jZ_k \sin \beta_k l_k \\ j \sin \beta_k l_k / Z_k & \cos \beta_k l_k \end{bmatrix} \qquad (3)$$

Solving for the transmission and reflection coefficients,

$$T = \frac{E_4^+}{E_0^+} = \frac{2}{A + B/Z_4 + CZ_0 + DZ_0/Z_4}$$
$$\Gamma = \frac{E_0^-}{E_0^+} = \frac{A + B/Z_4 - CZ_0 - DZ_0/Z_4}{A + B/Z_4 + CZ_0 + DZ_0/Z_4} \qquad (4)$$
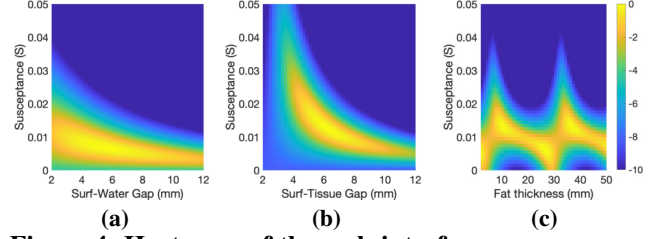
Figure 4: Heatmaps of through-interface power vs. surface admittance and environmental variation. The desired surface admittance varies with **(a) (b)** the surface-interface gap size or **(c)** the fat layer thickness. This highlights the necessity of surface programmability.

Compared to Equation 1, the propagation behavior at the interface is no longer solely decided by the medium impedance.

Other medium interfaces. Tissue is the most complex medium due to its layered structure of multiple substances, with non-uniform consistency. The above analysis can be applied to other medium combinations easily, e.g., air-water and air-ground interfaces, which involve matching only two media and are simpler cases than air-tissue interfaces.

Summary. The metasurface alters propagating signals and interacts with the media via its *surface admittance*, as in Equation 3. Therefore, it can change the transmission and reflection coefficients of the medium interface in Equation 4. This offers the knob to match the impedance of different media. However, there are numerous deployment specific factors such as surface-interface gap, medium composition and layer consistency, which motivate dynamic surface configuration.

3.2 Design Challenges and Requirements

Lightweight design for practicality. The optimal solution for medium impedance matching can be derived analytically with three layers of non-programmable metasurfaces [65]. However, a 3-layer surface, fitted at the medium interface, is cumbersome for deployment; We would need to cope with the surface substrate thicknesses and ensure a certain spacing between adjacent layers to avoid unwanted coupling. Instead, we aim for a single-layer design, which offers simplicity, low hardware cost, and minimal thickness for mechanical flexibility. Our calculation suggests a single layer is already able to achieve near-optimal impedance matching (less than 1 dB loss). Further, instead of requiring a fixed or no surface-interface gap, we decouple the surface placement from the interface position, allowing a varying surface-interface gap.

Appropriate admittance for matching. To achieve good medium impedance matching, the metasurface should have an appropriate surface admittance. We use the circuit model to numerically model signal propagation in diverse deployment scenarios. For any given surface admittance Y_s, we can calculate the ABCD matrix (Equation 3), and then the transmission

and reflection coefficients (Equation 4). Figure 4 shows the power transmitted through the medium interface when using different surface admittance values in scenarios with various surface-medium gap sizes or fat thicknesses. The higher the through-interface power, the lower the reflection, and thus, the better the medium matching performance. We can achieve near-optimal through-interface transmission (only 0.5 dB loss) by using an appropriate surface admittance ranging from 0 to over $0.05j$. However, such a large surface admittance range is challenging since drastically different surface patterns are often needed to cater to less than $0.01j$ change [64].

Dynamic adaptation for robustness. Based on the previous analysis, there is no one-size-fits-all surface admittance value. Several factors affect the appropriate surface admittance for impedance matching (Figure 4): (i) The gap between the surface and medium interface, hardly controllable in practice. The smaller the gap, the larger the admittance to maintain a high through-interface transmission power. (ii) Different medium pairs, medium composition and consistency. An air-tissue interface needs a much higher admittance than an air-water interface. Moreover, the fat thicknesses vary significantly from one person to another and even between different body parts of the same person, which affect the needed admittance significantly. (iii) The previous circuit model analysis and simulations used an approximate tissue model and lab-measured medium parameters, both simplified from real scenarios. The remaining systematic errors could degrade the surface performance by 2-3 dB, and we can use surface programmability to account for that.

Thus, we aim to design a single-layer programmable metasurface covering the desired surface admittance tuning range, from $0j$ to over $0.05j$. This provides sufficient programmability to adapt to the above dynamics and achieve robust performance, as confirmed experimentally in Section 5.4.

Operational frequencies. We focus on 2.4 GHz, but the design can be adapted to other frequencies like 900 MHz or 5 GHz by scaling the geometry of the metallic patterns. Several proposals [16, 35, 69] exploit 2.4 GHz Wi-Fi and bluetooth radios as ambient signal sources to provide backscatter connectivity. This could significantly lower the hardware requirement and make in-vivo networking more accessible for daily use. Moreover, the antenna size is inversely proportional to the frequency, and the small antenna size of 2.4 GHz is crucial for in-vivo devices [52].

3.3 Hardware Design

Surface elements. Our surface design consists of an array of basic repeating units as *elements*, each with two rectangular patches connected by varactor diodes (Figure 5(a)). This simple yet effective surface pattern is inspired by designs for other purposes [23, 61, 62]. The metallic patches act like antennas,

(a)

(b)
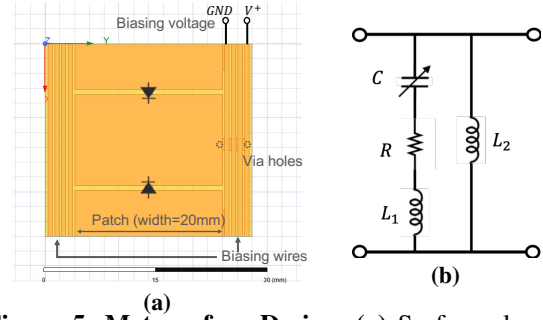
Figure 5: Metasurface Design. (a) Surface element. **(b)** Equivalent LC circuit. We control the voltage applied to varactor diodes with individual biasing wire for each element.

Table 2: Varactor performance vs reverse bias voltage.

| Voltage (V)	30	20	15	10	5	0
Capacitance (pF)	0.71	0.81	0.90	1.0	1.32	3.72
Resistance (Ω)	0.26	0.3	0.36	0.38	0.45	0.63

resonating with incident signals and inducing surface currents. The varactor diodes work as tunable capacitors, controlled by biasing voltages, to alter the electronic responses and produce the desired surface admittance. All surface elements share a common ground wire as the voltage reference, while each element has a separate biasing wire, connected through via holes. This permits element-wise surface admittance control for both medium impedance matching and beamforming.

Achieving programmability. The equivalent circuit for the surface element is shown in Figure 5(b), where C is the tunable capacitance of the varactor, R is the resistance of the varactor, L_1 is the inductance of each patch, and L_2 is the inductance of biasing wires. The surface admittance is

$$
\begin{aligned}
Y_s &= \frac{1}{\frac{1}{j\omega C} + R + j\omega L_1} + \frac{1}{j\omega L_2} \\
&= \frac{\omega^2 C^2 R + j\omega C(1 - \omega^2 CR)}{(1 - \omega^2 CL_1)^2 + (\omega CR)^2} - \frac{j}{\omega L_2} \\
&\approx \frac{\omega^2 C^2 R}{(1 - \omega^2 CL_1)^2} + \left(\frac{\omega C}{1 - \omega^2 CL_1} - \frac{1}{\omega L_2}\right)j
\end{aligned}
\tag{5}
$$

For our design, we have $(\omega CR)^2 \ll (1 - \omega^2 CL_1)$, thus allowing for the approximation in the last step. We observe that the tunable capacitance C is the dominant factor for the susceptance (the imaginary part of admittance), which enables programmability. The conductance (the real part of admittance) is proportional to the resistance R, which causes additional power loss on the surface. To minimize the loss and maximize tunability, we need to use varactors with a small resistance but a large capacitance tuning range.

Achieving desired admittance range. Our surface design needs to expose the desired tunable admittance range mentioned above; Otherwise, impedance matching cannot be achieved whatever the surface tuning algorithm. The surface
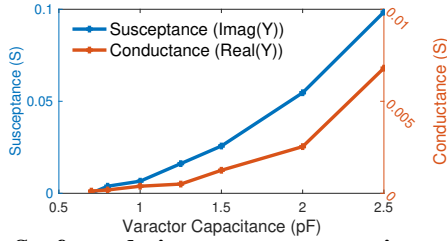
Figure 6: Surface admittance versus capacitance. Increasing the varactor capacitance also increases the surface admittance; The real (lossy) part of admittance is kept low.

admittance range depends on the geometry of the metallic pattern, the specific choice and placement of the varactors, the wiring between components, and how the biasing voltage is applied. The limited capacitance tuning range of varactors is also a hard constraint.

Specifically, we choose SMV1405 [9] varactor diodes and run SPICE [10] simulations to derive the capacitance and resistance verses bias voltage (Table 2). Given the varactor and its capacitance range, we derive a specific surface metallic pattern to achieve the desired admittance, guided by Equation 5. To increase the ratio of susceptance and varactor capacitance, we can lengthen the surface patch for higher L_1; To decrease the susceptance by a constant, we can increase the width of the biasing wire for lower L_2. Through iterative HFSS [1] simulations, we arrive at the final pattern shown in Figure 5(a). The pattern geometry is precisely tuned, e.g., a pattern 2 mm smaller in width and length has only half of the tunable admittance range and shifts the range partly to negative admittance values. Previous varactor-based metasurfaces lack considerations for our problem and cannot be used; They may have a small tunable surface admittance range anywhere in the entire design space, $-\infty j$ to ∞j, far off the desired range.

This way, we have a programmable metasurface that suits various situations, obviating environment-specific, non-programmable surfaces. We plot the surface admittance for different varactor capacitance values in Figure 6. The susceptance varies from $0j$ to over $0.05j$, while the conductance remains one order of magnitude lower than the susceptance. This shows we indeed achieve a large admittance tuning range while maintaining a low power loss on the surface. We primarily use the 0-2 pF capacitance range, because higher capacitance leads to higher resistance power loss and non-uniform admittance values over the 2.4 GHz band frequency range, both degrading matching performance.

Impedance matching simulation. To verify the medium impedance matching performance, we run HFSS [1] simulations for surfaces placed near air-tissue and air-water interfaces. First, we examine the reflection power changes as shown in Figure 7. With an appropriate capacitance of varactors (around 1 pF), the surface can achieve over 10 dB

(a) **(b)**
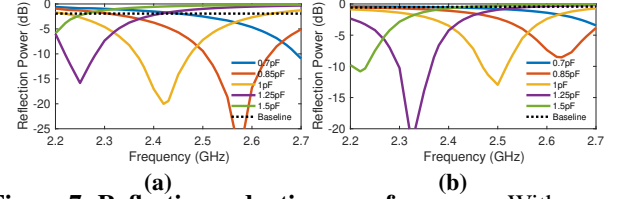
Figure 7: Reflection reduction over frequency. With appropriate varactor capacitances, the surface reduces the reflection by over 10 dB for **(a)** water and **(b)** tissue at around 2.4 GHz.
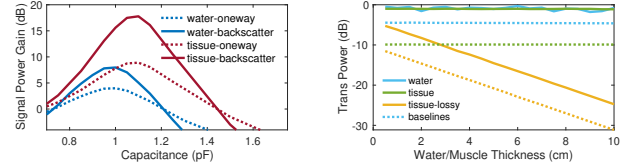
Figure 8: Cross-medium transmissive power gain.

Figure 9: Power gain at various in-vivo depths.

of reflection reduction and a sufficient bandwidth around 2.4 GHz for both water and tissue. The reflection trough shifts to neighboring frequencies when the capacitance of varactors is slightly different. The power transmitted through the interface exhibits a reversed trend over frequency, i.e., higher transmissive power with an appropriate capacitance. We show the transmission power gain versus capacitance in Figure 8, with a max gain of 4 dB and 9 dB for air-water and air-tissue links, respectively. Almost all incident power is transmitted through, but the air-tissue interface has a worse baseline power, resulting in a higher gain.

Our surface provides equal gains for both propagation directions by matching the medium impedance. Assuming the scattered signal strength is proportional to the strength of signals reaching a backscatter device [28], the backscatter power gain equals the sum of (dB-scale) gain values in two directions. We achieve gains of up to 8 dB and 18 dB for backscatter devices in water and tissue respectively. Next, we simulate the effect of endpoint depth (distance from the medium interface to the endpoint) and medium conductivity in Figure 9. We run other simulations with no conductivity to isolate the performance of medium impedance matching, but the experimental evaluation section naturally includes the influence of conductivity. For both air-water and air-tissue, the transmissive power gain remains constant regardless of the in-vivo endpoint depth. If we consider medium conductivity, the received power decreases when depth grows, while our surface provides a high gain regardless.

We further simulate the programmability provided by the varactors with a varying surface-interface gap and a varying fat layer thickness. Our surface design maintains a high power transmitted through the interface by choosing suitable capacitance values. The distribution of appropriate capacitance values matches the distribution of admittance values in Figure 4, consistent with the theoretical model.

Surface size. Given the per-element pattern, we need to decide the size of surface, i.e., how many repetitive elements. The previous simulations assume an infinite surface, while a finite surface may have different properties. We verify with simulations that a surface with 4×4 elements suffices. Once above this minimum element count, the size of the surface should match the application scenarios. A larger surface can provide a larger coverage area and higher beamforming gain, such as when made as a blanket for medical monitoring.

Beamforming. Endpoints in challenging media, such as water or tissue, often experience destructive multipath fading [59]. Since medium impedance matching only boosts the transmission through the metasurface and medium interface, further signal propagation can still be susceptible to multipath effects (Figure 13). Fortunately, we can apply a distinct biasing voltage to control per-element matching behavior, which provides element-wise on-off amplitude control on through-surface signals, without additional onboard RF switches. This is a separate functionality leveraging the element-wise impedance-matching capability to mitigate multipath fading, achieving beamforming gain on top of medium matching gain. Our single-layer design does not have the full range of phase control for beamforming, although it is achievable with more layers stacked. Previous work already discussed the performance margin [14], so we choose a one-layer design for its simplicity and deployability.

Surface shape and coupling. Substrate shape perturbations affect the beamforming performance, but not the impedance matching functionality; The surface admittance range, primarily influenced by the metallic pattern dimensions, is not sensitive to the substrate shape. This resilience is akin to flexible antenna designs, where shape perturbations minimally affect the resonance frequency, a principle observable in metamorphic surfaces [67]. Simulations across several substrate shapes, including elliptical configurations, confirm negligible impedance matching discrepancies against planar counterparts. A more drastic shape deformation like folding or rolling the surface [41], does not match our intended application scenario. Nonetheless, unexpected coupling between the surface and the non-air medium can occur when they are placed in proximity, diverging from theoretical circuit model predictions. A thick PCB substrate can reduce potential coupling, but at the cost of increased bulk and weight [64]. Fortunately, the surface programmability allows for adjustments to counteract any coupling effects.

3.4 Control Algorithm

We present a multi-stage algorithm to determine element configurations. First, it explicitly performs coarse-grained medium impedance matching to reduce the search space; Second, it performs beamforming based on the medium matching results; and Lastly, it performs fine-grained voltage tuning to adjust both the impedance and beamforming performance. Eventually, a portion of the surface elements *transmit* signals with medium impedance matching, while the rest *reflect* signals that would produce destructive multipath fading.

Channel model. We consider the multipath channel between the TX (transmitter) and the RX (receiver)

$$h_{T-R} = h_{env} + \sum_{i=1}^{i=N} s(V_i) \, h_i \tag{6}$$

where h_{env} is the collective channel coefficient representing all signal paths not going through the surface, N is the number of surface elements, $s(V_i)$ is a complex number representing the amplitude and phase changes caused by impedance matching effect of surface element i, V_i is the voltage applied, and h_i is the channel coefficient characterizing all paths going through element i. The goal is to set appropriate surface configurations, i.e., the voltage for each surface element, to maximize the received signal strength $\|h_{T-R}\|$ based on the endpoint feedback of the received signal strength.

Challenges. The optimal surface performance arises from both medium impedance matching and beamforming. However, there is no way to completely tease apart these two effects from the endpoint perspective. Further, the effect of impedance matching, $s(V_i)$, is not a fixed function of the voltage applied, V_i, that can be measured in advance; Many factors affect medium impedance matching as discussed in Section 3.2. Finally, a brute-force search enumerating all surface configurations is impractical; Considering our implementation, 8 discrete voltages each for 64 surface elements, the search space (8^{64}) is too large. Further, this is not a convex optimization problem as multiple local and global optima can exist. Given the specific challenges here, existing surface control algorithms, such as what RFocus [14] uses or a black-box optimization, do not work due to lacking both software and hardware considerations for cross-medium challenges.

Multi-stage solution. We divide and conquer this problem with a multi-stage control algorithm that performs medium impedance matching, beamforming, and refinement successively. In the first stage, we explicitly probe the medium matching performance, $s(V)$, to reduce the search space by applying a uniform voltage V to all surface elements. The channel equation above can be written as

$$h_{T-R} = h_{env} + s(V) \sum_{i=1}^{i=N} h_i \tag{7}$$

With a high probability, $\sum_{i=1}^{i=N} h_i$ is much larger than noise. The changes in $s(V)$ can be observed from the changes in h_{T-R} with different voltages applied. We record the two voltage states, V_1 and V_0, that respectively maximizes and minimizes the endpoint signal strength ($\|h_{T-R}\|$), as the input for

the next stage. Note that without knowing how the signal phase is aligned with h_{env}, we can not tell which state is maximizing $\|s(V_i)\|$ or minimizing it. Fortunately, we only need to know that these two states create the opposite effects.

In the second stage, we use the recorded states, V_1 and V_0, as on-off control for beamforming. We perform a majority voting procedure to find the best on-off configuration. Specifically, we want to determine the sets of elements adopting the on and off states respectively, S_1 and S_0. The channel we want to improve can be re-written as

$$h_{T-R} = h_{env} + s(V_0) \sum_{i \in S_0} h_i + s(V_1) \sum_{j \in S_1} h_j \qquad (8)$$

We batch test random on-off configurations of the surface and record the corresponding received signal strength from endpoint feedback. After testing all configurations, we count votes for each surface element. If a configuration leads to a higher signal strength than the median strength of all configurations, we cast a vote for each turned-on element in this configuration. Otherwise, we cast a vote for each turned-off element. An element is marked as *on* (S_1) if it receives votes from more than half of the tested configurations, or *off* (S_0) otherwise. For our surface prototype with 64 elements, we set the batch test number to 128 random configurations, which is significantly fewer than all 2^{64} possibilities. Setting the number of random configurations to twice the number of elements achieves a good balance between performance and feedback overhead; The extra gain of testing more configurations diminishes empirically. Figure 21 experimentally compares this algorithm with enumerating all configurations.

In the third stage, we refine V_1 and V_0 by testing the respective adjacent voltage values without changing the on-off element sets, S_1 and S_0. We update V_1 and V_0 for the respective element sets if a higher received signal strength is achieved. This aligns the phase of h_{env} with that of through-interface signals and accounts for any inaccuracy in stage one.

Control granularity. We use 8 voltage values (30, 20, 15, 10, 5, 2.5, 0) in the control algorithm. These values are chosen empirically to cover the tunable surface admittance range. Using more voltage values can bring additional performance gain, but requires more feedback measurements. Another design choice about control granularity is that we utilize element-wise control of the surface. Figure 21 shows the extra gain from element-wise control over column-wise control.

Feedback mechanism. We use the received signal strength (RSS) as the feedback signal to guide our algorithm, which is accessible across diverse wireless hardware. Due to the reciprocity of metasurface operations, feedback from either end of the cross-surface link is sufficient; We use feedback from in-air devices only, avoiding overhead for in-body or in-water devices. We can potentially avoid feedback by incorporating sensing hardware as in LAVA [68]. For backscatter devices,
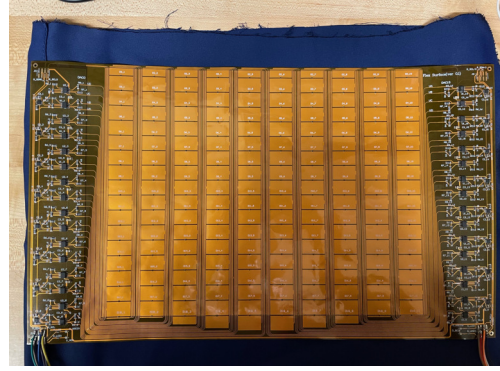
(a) Surface prototype as a flexible PCB. The control circuit is currently placed on the sides to ease soldering. Further circuit integration can enable a smaller form factor.
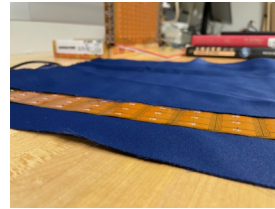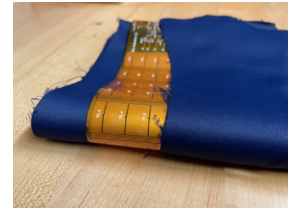
(b) 0.1 mm in thickness.   **(c) As flexible as fabric.**

Figure 10: Surface hardware implementation.

we use the received backscatter signal strength measurement from the in-air endpoint, similar to In-N-out [28]. There is usually a margin between sufficient RSS for useful links and minimum detectable RSS for feedback. When endpoints are undetectable initially, we can potentially perform blind impedance matching and beamforming, using sub-optimal configurations to power up (backscatter) devices.

4 IMPLEMENTATION

Surface Fabrication. We fabricate the surface using commercial flexible PCB fabrication process and manually solder circuit components including the SMV1405 varactors [9] (Figure 10(a)). A surface prototype is as thin as a piece of paper, about 0.1 mm thick (Figure 10(b)), and as flexible as fabric (Figure 10(c)). This facilitates flexible surface deployment, e.g., as a metasurface blanket or T-shirt for medical monitoring. Additional plastic lamination can waterproof the surface for diverse scenarios. Due to limitations of the fabrication process, the area size of our surface prototypes is capped at 24×40 cm, with 8×10 elements. We individually control the voltages of 64 elements, while the remaining 16 act as padding to avoid surface edge effects. Fabricating each piece of surface costs $50 and the circuit components cost around $100, $1.5 per tunable element. The cost can be much lower for large scale production due to economies of scale.

Control Circuit. Since varactors hardly draw any current, we design a lightweight varactor voltage control circuit. For a

smaller system form factor than previous work [23, 24, 29], we integrate the control circuit on the surface to avoid external DAC devices. Our implementation uses 16 4-channel DAC MPC4728 chips [8], each connected to two LM358 OP amplifiers [6] to amplify the voltage from 0–4 V to 0–36 V. We prioritize the ease of soldering for the current PCB layout, while a highly integrated circuit implementation can achieve a smaller form factor. A PC with Intel I7-7700 acts as the controller, collecting feedback and computing surface configurations with Matlab; These are then sent to an ESP32 [3] over Wi-Fi to configure the DAC chips through two I2C buses.

Control latency. The speed of control dictates whether our system can react promptly to environmental dynamics and multipath fluctuations within each medium. In the high speed mode, each I2C bus in our control circuit provides a bandwidth of 3.4 Mbps [8]. It takes 9 bytes to transfer the voltage data to one chip, so only 0.17 ms to set 16 chips using 2 buses. Our control algorithm goes through 3 exploration stages, which requires 8, 128, and 9 tests of surface configurations respectively. Hence, our system can explore the search space in less than 25 ms. This is well within the channel coherence time for most scenarios and enables mobility support with real-time adaption, although we do not explicitly optimize for endpoint mobility in the current implementation.

Power consumption. Our surface design is passive and consumes little power. The varactors are reverse-biased and draw a maximum of 20 nA of reversed current [9], or less than 1.2 uW power per surface element under a 30 V bias voltage. The power consumption of all surface elements in our implementation is less than 100 uW, close to the power footprint of many backscatter designs [16, 69], within the capability of ambient signal power harvesting. Our control circuit is currently designed for precise voltage control to validate and characterize the surface, not optimized for power consumption; More specialized circuit designs can reduce power consumption significantly, for example, by using low-power circuits providing selected discrete voltages instead of DACs. This is beyond the scope of this paper.

5 EVALUATION

We first validate the medium impedance matching capability of RF-Mediator and then evaluate its end-to-end performance gain. To highlight the benefits of programmability, RF-Mediator is compared with a non-programmable surface when subjected to environmental dynamics. We also perform microbenchmarks of system operations and effectiveness.

5.1 Experiment Setup

Media studied. We mainly study the performance of RF-Mediator for air-water and air-tissue (emulated with pork belly) links. The property of ground (soil) is dictated by the

(a)   **(b)**
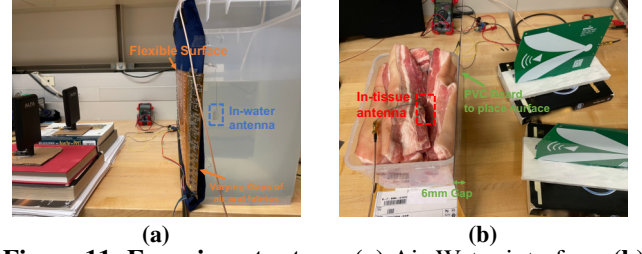
Figure 11: Experiment setups. (a) Air-Water interface. **(b)** Air-Tissue (pork belly) interface. We use fabric layers or a plastic board to host the surface; fabric and plastic exhibit similar permittivity to air compared to water or tissue.



(a) Water   **(b) Tissue**
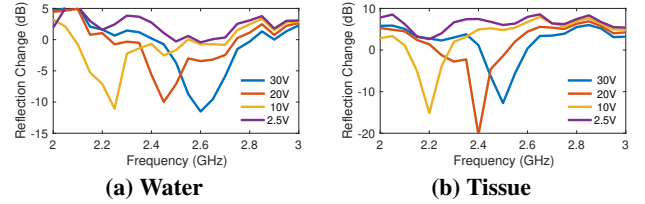
Figure 12: Reflection reduction over frequency. Matching medium impedance reduces reflection by over 10 dB. The biasing voltage should be set to match the center frequency of the links (the red line, trough showing minimal reflection).

water it contains [54], so we expect the performance for air-to-ground links to be similar to air-to-water links. We place water and pork belly in plastic containers (Figure 11) and place the surface in front of the test medium with a default air gap of 5 mm. Although there are fabric layers and a plastic container between the surface and the other test medium, they exhibit similar permittivity to air, in contrast to water and tissue [2, 63]. Moreover, fabric layers are not solid material and most of their volume is taken up by air. Thus, they can be treated as air in terms of the medium-specific signal propagation behavior.

We conduct most experiments with a water container (Figure 11(a)), as it is much easier to experiment with and sample endpoint locations inside water than tissue. The container is similar to human upper body in size, so we can emulate air-to-tissue links for medical devices. Impedance matching for air-water and air-tissue interfaces follows the same principle, as described in Section 3.1, and both water and tissue experience similarly difficult channel conditions [42]. Nevertheless, to further verify the system, we show the performance gain for air-tissue links in Figure 14 and Figure 20.

Link setup. We set up 2.4 GHz links for experiments using USRP N210s [4] unless otherwise noted. We use directional patch antennas [46] for in-air endpoints and (water-proof) omni-directional flexible antennas [5] for in-water and in-tissue endpoints (connected to the USRPs with coaxial cables). To sample various channel conditions, we move both endpoints, creating different incident angles for the incoming signal to the medium interface, at up to 45 degrees. We use the received signal strength (RSS) of the in-air endpoint as

(a) Water   **(b) Tissue**
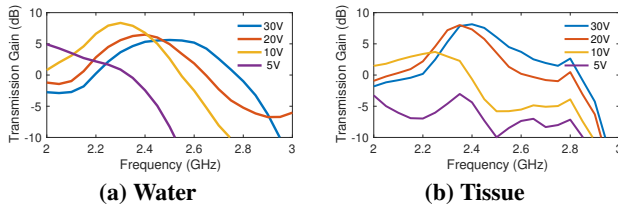
Figure 13: Transmissive power gain over frequency. With an appropriate voltage, impedance matching increases through-interface power by over 5 dB, although multipath reflections inside the water/tissue containers affect results.

feedback for all experiments, as it is easier to obtain than any information from the in-water or in-tissue endpoints. Due to channel reciprocity, the channel feedback in both directions only differs by a constant in our experiments, so both can guide the surface control algorithm and yield similar results. For all experiments, we remove the surface to measure a faithful baseline received power.

Surface shapes. Controlling flexible surface shape perturbations precisely and repeatably is very difficult. However, in our experimental setup, random shape perturbations arise as surfaces are removed (and redeployed) for baseline measurements across different links. We model such perturbation implicitly as channel variation and rely on surface programmability to address it. Moreover, for all experiments with the water container, our surface prototype naturally took on a curved shape as shown in Figure 11(a). This curvature results from the container's deformation under the weight of the water, up to 40 qt and weighing over 70 lb when full. Such macroscopic shape perturbation, akin to a blanket covering the stomach of an individual lying on their back, represents typical deployment scenarios.

5.2 Medium Impedance Matching Validation

We first verify the fundamental hardware functionality, i.e., medium impedance matching. To avoid conflating with the control algorithm performance, we manually apply selected voltage to all surface elements uniformly here to focus on the matching performance without the additional beamforming gain. We place RF absorbing foam [7] around the setup to minimize multipath effects (for this experiment only).

Reflection reduction. We first measure the reduction of reflection power from the medium interfaces. We set up a short link using two directional Vivaldi antennas, around 30 cm apart, both pointing towards the surface and the water/tissue containers at a small angle (Figure 11(b)). This distance roughly ensures we only measure the most direct reflection path from the surface and medium interface. We measure the reflection power strength when the surface is deployed and subjected to different bias voltages. Figure 12 shows the surface reduces the reflection by over 10 dB around 2.4 GHz,

compared to the surface-free baseline, for both air-water and air-tissue interfaces. This shows that appropriate voltages can result in good medium impedance matching, i.e., large reflection reduction, agreeing with the results in Figure 7. The shift of matching troughs with decreasing voltage also agrees with Figure 7, which indicates an increased surface admittance as expected when the voltage decreases. The exact voltage needed (20 V) for medium impedance matching on 2.4 GHz is different from the simulated value (10 V). This is because simulations rarely capture practical deployments perfectly, due to real-world constraints like surface-medium gaps and varying tissue layer composition and consistency.

Through-interface transmission boost. The reduction in reflection should correspond to an increase of through-interface signal power. Figure 13 verifies this through the received signal power gain on the in-water and in-tissue antennas. Without running our control algorithm, we see over 5 dB in power gain when an appropriate voltage is selected, which matches Figure 8. The reflection power from the medium interface is stronger and easier to measure, while the in-water or in-vivo received signal power is susceptible to multipath fading inside the container, leading to irregular curves; Thus, we expect only a qualitative match-up. This highlights the necessity of dynamic surface adaptation to counter multipath effects and other environmental changes.

5.3 Boosting Cross-Medium Links

Next, we activate the control algorithm to assess the end-to-end link improvement from RF-Mediator, with gains from both medium impedance matching and beamforming.

Received signal strength gain. We experiment with 45 air-water and 30 air-tissue links. Specifically, we place the in-water antenna at 3 locations (5, 7.5, 10 cm away from the air-water interface inside the water container), 5 different locations each, while the in-air endpoint is placed at 3 locations (25, 35, 50 cm away from the metasurface). This is the default setup unless otherwise noted. RF-Mediator boosts the received signal power of in-water endpoints by a median of 7.2 dB and up to 22 dB (Figure 14). For air-to-tissue links, we experiment with 2 in-vivo endpoint locations and 15 in-air endpoint locations. The results show a median gain of 8.2 dB and up to 17.5 dB for the in-vivo received signal power. Thus, our system can effectively match the impedance between air and tissue despite the challenging multi-layer structure of tissue. To put the gain in context, the signal-to-noise ratio (SNR) of air-to-tissue links in a state-of-the-art medical prototype [52] is around 10 dB and can be negative due to channel variation. RF-Mediator provides extra link budget, enabling longer and more reliable links or higher throughput.
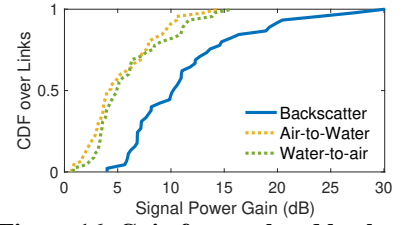
Bi-directional gain. Figure 14 shows the received signal power gain from water or tissue to air, i.e., the reversed link
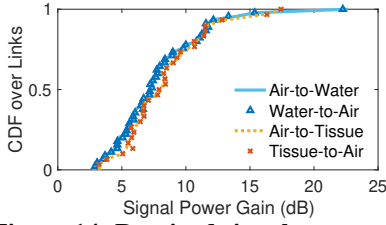
Figure 14: Received signal power gain for bi-directional cross-medium links.
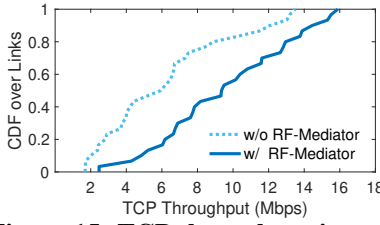
Figure 15: TCP throughput improvement for air-water Wi-Fi links.

Figure 16: Gain for emulated backscatter links.

direction. The gains in both directions match well for individual links, confirming direction-agnostic gains due to channel reciprocity. The gain for tissue-air links is higher than for water-air links. This agrees with the simulation results in Figure 8, but the extra gain is smaller for several possible reasons. We use multiple pieces of pork belly to construct the in-vivo environment, inadvertently leaving some air gaps (air-based propagating paths) in between. This can produce a higher surface-free baseline power, thus lowering the gain from the surface. Another reason is that each piece of pork has a different fat layer thickness, creating challenging discontinuities in the medium composition for impedance matching.

Throughput improvement. To show the throughput increase brought by the signal power gain, we measure TCP throughput with `iperf` for 45 air-to-water Wi-Fi links with and without the surface. The air-water links are set up as mentioned above, except that we use the widely used IoT hardware, ESP32 [3], as the endpoints. The Wi-Fi RSSI from the in-air endpoint is the feedback to the control algorithm. We place a flexible antenna [5] in the water as the in-water endpoint, and connect it to an ESP32 via a cable . The transmit power is set to 0 dBm to emulate devices with a tight power budget, following [52, 68]. Figure 15 shows our surface achieves a median throughput increase of 55%, and up to about 400%.

Backscatter links. As discussed in Section 2.1, we expect up to double the gain seen above for backscatter links since the signals traverse the medium interface twice. We use 2 USRP N210s as the in-air transmitter and receiver, and another USRP connected to a flexible antenna in the water as the backscatter device. Existing backscatter devices often shift the backscatter signal frequency to avoid self-interference [16, 35, 59]. Thus, we shift the backscatter-to-receiver channel (central frequency) by 20 MHz relative to the transmitter-to-backscatter channel. This means our system needs to support two separate channels simultaneously. Since backscatter signals traverse both channels until reaching the receiver, we multiply the channel coefficients in both directions to emulate the overall channel coefficient of backscatter links. Here, we assume the backscatter signal power is proportional to the incident power [28, 59]. Our control algorithm takes the amplitude of the overall channel coefficient as feedback to match practical settings. We place the in-air transmitter and

in-air receivers at 3 locations and test 15 in-water backscatter locations, measuring 45 links in total. Figure 16 shows RF-Mediator provides a median gain of 10.3 dB and up to 30 dB for the final received signal power. The gain comes from both the transmitter-to-backscatter (air-to-water) and backscatter-to-receiver (water-to-air) directions.

Endpoint-surface distance. As the surface can not cover the whole medium interface, only part of the incident signals traverses through the surface. We set up 15 air-to-water links, varying the distance between the surface and the in-air endpoint. Figure 17 shows the performance degrades slowly over distance but still boosts the through-interface power.

5.4 Benefits of Programmability

Programmability gain breakdown. We perform ablation study on RF-Mediator by gradually removing its programmability capability (Figure 18). For reference, RF-Mediator provides a median gain of 7.4 dB for 45 air-water links. If we omit element-wise beamforming control and instead apply uniform voltage to all elements, dynamic medium impedance matching alone provides a median gain of 4.5 dB. This roughly matches the results in Figure 13(a), but is more affected by the specific multipath channels. If we further remove dynamic voltage control and instead use a fixed, pre-determined best voltage (15 V) for all links, such a "non-programmable" surface yields only a median gain of 2 dB. The non-programmable surface also incurs up to 7.6 dB of power *loss* due to channel variation, significantly affecting the system usability, while RF-Mediator provides at least 3 dB gain for *all* links by adapting to the channel (i.e., applying dynamic voltage settings). This shows that surface programmability provides a beamforming gain and handles channel fluctuations effectively.

Robustness to surface-interface gaps. We evaluate system performance when adapting to a varying gap, produced by different numbers of fabric layers, between the surface and the water container. Each fabric layer adds around 2 mm and the container wall is around 1 mm thick. We test 0 to 4 fabric layers, i.e., 1 to 9 mm gap, with 30 air-to-water links each. Figure 19 shows a median gain of over 5 dB of and up to 15 dB for all gap sizes, which demonstrates the effectiveness of surface adaptation. Theoretically, the largest
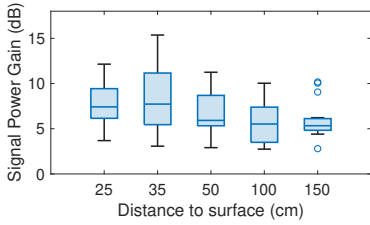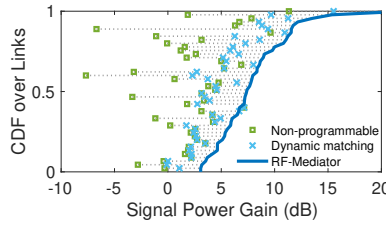
Figure 17: Surface-endpoint distance.
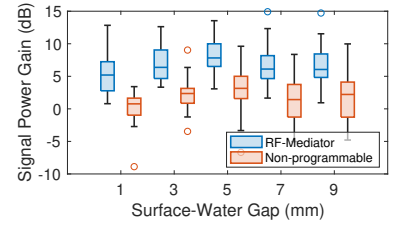

Figure 18: Need for programmability.
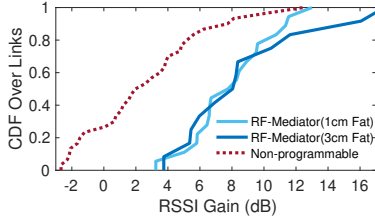

Figure 19: Surface-interface gap.

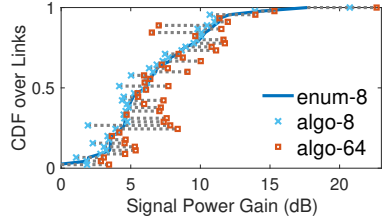**Figure 20: Adaptation for different fat thicknesses.**

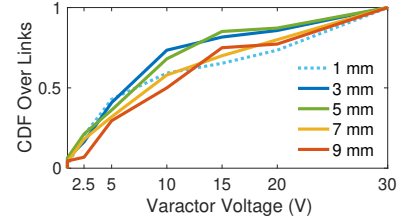**Figure 21: Algorithm variant comparison.**

Figure 22: Selected varactor voltage vs. surface-interface gap.

gap our design can cater to is up to 1.2 cm (Figure 4) without performance degradation; This is sufficient for most scenarios, for example, when the user is covered in a gown or blanket. The best performance is observed for the 5-mm gap, and the worst at 1 mm, which is consistent with Figure 4(a), but a high gain can be achieved regardless of gap size. For a non-programmable surface that applies a (best-matched) uniform voltage to all elements, its median gain is around 5 dB lower than RF-Mediator and the worst-case performance incurs over 10 dB power loss. This again confirms the need to adapt to environmental fluctuations.

Robustness to fat layer thickness. The thickness of the fat layer affects the capacitance needed for impedance matching (Figure 4(c)). We consider two in-vivo endpoint locations, behind a fat layer 1 cm and 3 cm in thickness respectively, and measure 15 air-tissue links for each. RF-Mediator provides high RSSI gains similarly for the two in-vivo locations despite different amounts of fat involved (Figure 20). As in previous setups, a non-programmable surface achieves a median gain over 5 dB lower than RF-Mediator, highlighting the benefit of adapting to medium consistency.

5.5 Control Algorithm Microbenchmarks

Beamforming near-optimality. Recall that for beamforming in stage two of our algorithm, we adopt fine-grained, element-wise control but prune the search space. Therefore, we assess the benefit of the former and the cost of the latter. We experiment with three algorithm variants, each over 45 air-to-water links: (i) Brute-force column-wise control, enumerating all configurations of 8 columns, with 2^8 channel measurements; (ii) our algorithm applied to column-wise adaptation of 8 columns, with 32 measurements only; and (iii) the RF-Mediator default, element-wise control of 64 elements, with 128 measurements. The first variant provides the

optimal result for 8 columns, while our 8-column algorithm exhibits near-optimal performance (Figure 21) but one-eighth the feedback measurements. Controlling 64 elements individually often provides extra gains of 2-3 dB compared to 8 columns, highlighting the benefit of element-wise control.

Voltage control effectiveness. We analyze the voltage values chosen in the first algorithm stage (Figure 22) to understand whether the control algorithm is operating as expected. The coupling between the surface and water affects the results with 1 mm gap due to the proximity, which is also observed in HFSS simulations. As the medium-interface gap increases from 2 mm to 9 mm, the median of the selected voltage increases from lower than 5V to 10V, indicating the corresponding varactor capacitance and surface admittance are decreasing. This descending trend agrees with our theoretical analysis and simulations results (Figure 4(a)).

6 CONCLUSION

Cross-medium wireless face the fundamental challenge of signal degradation when waves propagate through medium interfaces. In this paper, we present a lightweight programmable metasurface system, RF-Mediator, to tackle the root cause of the problem via novel device-protocol co-design. When placed at or near the medium interface, our metasurface dynamically mediates the media on both sides of the surface, as if no physical interface existed. Our prototype implementation on a single layer of thin and flexible plastic sheet is amenable to diverse applications. This provides an enabling technology for future IoT applications in challenging communication settings. Other applications of RF-Mediator include boosting in-air links, enhancing privacy against wireless sensing, and sensing the medium composition.

REFERENCES

[1] Ansys HFSS 3D High Frequency Simulation Software. https://www.ansys.com/products/electronics/ansys-hfss.

[2] DIELECTRICAL CONSTANTS OF POLYMERS. https://polymerdatabase.com/polymer%20physics/Epsilon%20Table.html.

[3] Epressif ESP32-DevKitC Board. https://www.espressif.com/en/products/devkits/esp32-devkitc.

[4] Ettus Research USRP N210. https://www.ettus.com/all-products/un210-kit/,.

[5] LairdConnect FlexNotch WiFi and Bluetooth Flexible 2.4 GHz Antenna. https://www.lairdconnect.com/rf-antennas/wifi-antennas/internal-antennas/flexnotch-24-ghz-antenna.

[6] LM358: Dual Operational Amplifier. https://www.ti.com/lit/ds/symlink/lm358.pdf.

[7] MAST Technologies Lossy Foam Absorber. https://www.masttechnologies.com/products/commercial/rf-absorbers-commercial/lossy-foam-0-5/.

[8] MPC4728: 12-Bit, Quad Digital-to-Analog Converter. http://ww1.microchip.com/downloads/en/devicedoc/22187e.pdf.

[9] SMV1405: Plastic Packaged Abrupt Junction Tuning Varactors. https://www.mouser.com/datasheet/2/472/200068N-15249.pdf.

[10] SPICE (Simulation Program with Integrated Circuit Emphasis). https://en.wikipedia.org/wiki/SPICE.

[11] Underwater Cultural Heritage. https://en.unesco.org/underwater-heritage.

[12] M. R. Abdelhamid, R. Chen, J. Cho, A. P. Chandrakasan, F. Adib. Self-reconfigurable micro-implants for cross-tissue wireless and batteryless connectivity. *Proceedings of the 26th Annual International Conference on Mobile Computing and Networking*, MobiCom '20, 1–14. Association for Computing Machinery, New York, NY, USA, 2020.

[13] D. R. Agrawal, Y. Tanabe, D. Weng, A. Ma, S. Hsu, S.-Y. Liao, Z. Zhen, Z.-Y. Zhu, C. Sun, Z. Dong, F. Yang, H. F. Tse, A. S. Y. Poon, J. S. Ho. Conformal phased surfaces for wireless powering of bioelectronic microdevices. *Nature Biomedical Engineering*, **1**(3), 1–9, 2017.

[14] V. Arun, H. Balakrishnan. RFocus: Practical Beamforming for Small Devices. *Symposium on Networked Systems Design and Implementation (NSDI)*, 1047–1061. USENIX, 2020.

[15] L. Bandyopadhyay, S. Chaulya, P. Mishra. Wireless communication in underground mines. *RFID-Based Sens. Netw*, **22**, 2010.

[16] D. Bharadia, K. R. Joshi, M. Kotaru, S. Katti. Backfi: High throughput wifi backscatter. *ACM SIGCOMM Computer Communication Review*, **45**(4), 283–296, 2015.

[17] J. Blauert, A. Kiourti. Bio-Matched Antennas With Flare Extensions for Reduced Low Frequency Cutoff. *IEEE Open Journal of Antennas and Propagation*, **1**, 136–141, 2020.

[18] J. Blauert, A. Kiourti. Theoretical Modeling and Design Guidelines for a New Class of Wearable Bio-Matched Antennas. *IEEE Transactions on Antennas and Propagation*, **68**(3), 2040–2049, 2020.

[19] E. Bok, J. J. Park, H. Choi, C. K. Han, O. B. Wright, S. H. Lee. Meta-surface for Water-to-Air Sound Transmission. *Phys. Rev. Lett.*, **120**, 044,302, 2018.

[20] A. Burton, S. N. Obaid, A. Vázquez-Guardado, M. B. Schmit, T. Stuart, L. Cai, Z. Chen, I. Kandela, C. R. Haney, E. A. Waters, H. Cai, J. A. Rogers, L. Lu, P. Gutruf. Wireless, battery-free subdermally implantable photometry systems for chronic recording of neural dynamics. *Proceedings of the National Academy of Sciences*, **117**(6), 2835–2845, 2020.

[21] H. Cano-García, P. Kosmas, E. Kallos. Enhancing electromagnetic transmission through biological tissues at millimeter waves using sub-wavelength metamaterial antireflection coatings. *2015 9th International Congress on Advanced Electromagnetic Materials in Microwaves and Optics (METAMATERIALS)*, 43–45, 2015.

[22] C. J. Carver, Z. Tian, H. Zhang, K. M. Odame, A. Q. Li, X. Zhou. AmphiLight: direct air-water communication with laser light. *Proceedings of the 17th Usenix Conference on Networked Systems Design and Implementation*, NSDI'20, 373–388. USENIX Association, USA, 2020.

[23] L. Chen, W. Hu, K. Jamieson, X. Chen, D. Fang, J. Gummeson. Pushing the physical limits of IoT devices with programmable metasurfaces. *Symposium on Networked Systems Design and Implementation (NSDI)*, 425–438. USENIX, 2021.

[24] K. W. Cho, M. H. Mazaheri, J. Gummeson, O. Abari, K. Jamieson. mmWall: A steerable, transflective metamaterial surface for NextG mmWave networks. *20th USENIX Symposium on Networked Systems Design and Implementation (NSDI 23)*, 1647–1665, 2023.

[25] J. Ding, R. Chandra. Towards Low Cost Soil Sensing Using Wi-Fi. *The 25th Annual International Conference on Mobile Computing and Networking*, MobiCom '19, 1–16. Association for Computing Machinery, New York, NY, USA, 2019.

[26] A. H. Dorrah, M. Chen, G. V. Eleftheriades. Bianisotropic Huygens' Metasurface for Wideband Impedance Matching Between Two Dielectric Media. *IEEE Transactions on Antennas and Propagation*, **66**(9), 4729–4742, 2018.

[27] M. Dunna, C. Zhang, D. Sievenpiper, D. Bharadia. ScatterMIMO: enabling virtual MIMO with smart surfaces. *Proceedings of International Conference on Mobile Computing and Networking (Mobicom)*, 1–14. ACM, 2020.

[28] X. Fan, L. Shangguan, R. Howard, Y. Zhang, Y. Peng, J. Xiong, Y. Ma, X.-Y. Li. Towards flexible wireless charging for medical implants using distributed antenna system. *Proceedings of the 26th Annual International Conference on Mobile Computing and Networking*, MobiCom '20, 1–15. Association for Computing Machinery, New York, NY, USA, 2020.

[29] C. Feng, X. Li, Y. Zhang, X. Wang, L. Chang, F. Wang, X. Zhang, X. Chen. RFlens: metasurface-enabled beamforming for IoT communication and sensing. *Proceedings of the 27th Annual International Conference on Mobile Computing and Networking*, MobiCom '21, 587–600. Association for Computing Machinery, New York, NY, USA, 2021.

[30] C. Gabriel, S. Gabriel, E. Corthout. The dielectric properties of biological tissues: I. Literature survey. *Physics in Medicine & Biology*, **41**(11), 2231, 1996.

[31] S. Genovesi, I. R. Butterworth, J. E. C. Serrallés, L. Daniel. Metasurface Matching Layers for Enhanced Electric Field Penetration Into the Human Body. *IEEE Access*, **8**, 197,745–197,756, 2020.

[32] X. Guo, Y. He, Z. Yu, J. Zhang, Y. Liu, L. Shangguan. RF-transformer: a unified backscatter radio hardware abstraction. *Proceedings of the 28th Annual International Conference on Mobile Computing And Networking*, 446–458, 2022.

[33] T. Hao, W. Zheng, W. He, K. Lin. Air-Ground Impedance Matching by Depositing Metasurfaces for Enhanced GPR Detection. *IEEE Transactions on Geoscience and Remote Sensing*, **58**(6), 4061–4075, 2020.

[34] Z. Huang, S. Zhao, S. Zhang, Z. Cai, Z. Li, J. Xiao, M. Su, Q. Guo, C. Zhang, Y. Pan, *et al.* Tunable fluid-type metasurface for wide-angle and multifrequency water-air acoustic transmission. *Research*, 2021.

[35] V. Iyer, V. Talla, B. Kellogg, S. Gollakota, J. Smith. Inter-Technology Backscatter: Towards Internet Connectivity for Implanted Devices. *Proceedings of the 2016 ACM SIGCOMM Conference*, SIGCOMM '16, 356–369. Association for Computing Machinery, New York, NY, USA, 2016.

[36] H. M. Jol. *Ground Penetrating Radar Theory and Applications*. Elsevier, 2008.

[37] U. M. Khan, M. Shahzad. Estimating soil moisture using RF signals. *Proceedings of the 28th Annual International Conference on Mobile Computing And Networking*, MobiCom '22, 242–254. Association for Computing Machinery, New York, NY, USA, 2022.

[38] C. H. Lee, H. Kim, D. V. Harburg, G. Park, Y. Ma, T. Pan, J. S. Kim, N. Y. Lee, B. H. Kim, K.-I. Jang, S.-K. Kang, Y. Huang, J. Kim, K.-M. Lee, C. Leal, J. A. Rogers. Biological lipid membranes for on-demand, wireless drug delivery from thin, bioresorbable electronic implants. *NPG Asia Materials*, **7**(11), e227–e227, 2015.

[39] Z. Li, Y. Xie, L. Shangguan, R. I. Zelaya, J. Gummeson, W. Hu, K. Jamieson. Towards Programming the Radio Environment with Large Arrays of Inexpensive Antennas. *Symposium on Networked Systems Design and Implementation (NSDI)*, 285–300. USENIX, 2019.

[40] J.-j. Liu, Z.-w. Li, B. Liang, J.-c. Cheng, A. Alu. Remote Water-to-air Eavesdropping through Phase-Engineered Impedance Matching Metasurfaces. *arXiv preprint arXiv:2208.12999*, 2022.

[41] R. Ma, R. I. Zelaya, W. Hu. Softly, Deftly, Scrolls Unfurl Their Splendor: Rolling Flexible Surfaces for Wideband Wireless. ACM MobiCom '23. Association for Computing Machinery, New York, NY, USA, 2023.

[42] Y. Ma, Z. Luo, C. Steiger, G. Traverso, F. Adib. Enabling deep-tissue networking for miniature medical devices. *Proceedings of the 2018 Conference of the ACM Special Interest Group on Data Communication*, SIGCOMM '18, 417–431. Association for Computing Machinery, New York, NY, USA, 2018.

[43] G. Meron, A. Glukhovsky, P. Swain. Wireless capsule endoscopy. *Nature*, **405**.

[44] D. Nikolayev, M. Zhadobov, P. Karban, R. Sauleau. Electromagnetic Radiation Efficiency of Body-Implanted Devices. *Physical Review Applied*, **9**(2), 024,033, 2018.

[45] H. Pan, L. Qiu, B. Ouyang, S. Zheng, Y. Zhang, Y.-C. Chen, G. Xue. PMSat: Optimizing Passive Metasurface for Low Earth Orbit Satellite Communication. *Proceedings of the 29th Annual International Conference on Mobile Computing and Networking*, 1–15, 2023.

[46] Alpha Network Antenna APA-M25. https://www.alfa.com.tw/products_detail/234.htm.

[47] C. Pfeiffer, A. Grbic. Cascaded metasurfaces for complete phase and polarization control. *Applied Physics Letters*, **102**(23), 231,116, 2013.

[48] C. Pfeiffer, A. Grbic. Metamaterial Huygens' Surfaces: Tailoring Wave Fronts with Reflectionless Sheets. *Physical Review Letters*, **110**(19), 197,401, 2013.

[49] D. M. Pozar. *Microwave engineering*. John wiley & sons, 2011.

[50] K. A. Remley, G. Koepke, D. G. Camell, C. Grosvenor, G. Hough, R. T. Johnk. Wireless Communications in Tunnels for Urban Search and Rescue Robots. *Proceedings of the 8th Workshop on Performance Metrics for Intelligent Systems*, PerMIS '08, 236–243. Association for Computing Machinery, New York, NY, USA, 2008.

[51] N. M. Schuster, A. M. Rapoport. New strategies for the treatment and prevention of primary headache disorders. *Nature Reviews. Neurology*, **12**(11), 635–650, 2016.

[52] S. Sharma, K. B. Ramadi, N. H. Poole, S. S. Srinivasan, K. Ishida, J. Kuosmanen, J. Jenkins, F. Aghlmand, M. B. Swift, M. G. Shapiro, *et al.* Location-aware ingestible microdevices for wireless monitoring of gastrointestinal dynamics. *Nature Electronics*, **6**(3), 242–256, 2023.

[53] F. T. Sun, M. J. Morrell. Closed-loop Neurostimulation: The Clinical Experience. *Neurotherapeutics*, **11**(3), 553–563, 2014.

[54] L. Thring, D. Boddice, N. Metje, G. Curioni, D. Chapman, L. Pring. Factors affecting soil permittivity and proposals to obtain gravimetric water content from time domain reflectometry measurements. *Canadian Geotechnical Journal*, **51**(11), 1303–1317, 2014.

[55] X. Tian, Q. Zeng, S. A. Kurt, R. R. Li, D. T. Nguyen, Z. Xiong, Z. Li, X. Yang, X. Xiao, C. Wu, *et al.* Implant-to-implant wireless networking with metamaterial textiles. *Nature Communications*, **14**(1), 4335, 2023.

[56] F. Tonolini, F. Adib. Networking across boundaries: enabling wireless communication through the water-air interface. *Proceedings of the 2018 Conference of the ACM Special Interest Group on Data Communication*, SIGCOMM '18, 117–131. Association for Computing Machinery, New York, NY, USA, 2018.

[57] G. Traverso, G. Ciccarelli, S. Schwartz, T. Hughes, T. Boettcher, R. Barman, R. Langer, A. Swiston. Physiologic Status Monitoring via the Gastrointestinal Tract. *PLOS ONE*, **10**(11), e0141,666, 2015.

[58] D. Vasisht, Z. Kapetanovic, J. Won, X. Jin, R. Chandra, S. Sinha, A. Kapoor, M. Sudarshan, S. Stratman. FarmBeats: an IoT platform for Data-Driven agriculture. *14th USENIX Symposium on Networked Systems Design and Implementation (NSDI 17)*, 515–529, 2017.

[59] D. Vasisht, G. Zhang, O. Abari, H.-M. Lu, J. Flanz, D. Katabi. In-body backscatter communication and localization. *Proceedings of the 2018 Conference of the ACM Special Interest Group on Data Communication*, SIGCOMM '18, 132–146. Association for Computing Machinery, New York, NY, USA, 2018.

[60] A. Welkie, L. Shangguan, J. Gummeson, W. Hu, K. Jamieson. Programmable Radio Environments for Smart Spaces. *Workshop on Hot Topics in Networks (HotNets)*. ACM, 2017.

[61] Z. Wu, Y. Ra'di, A. Grbic. Tunable Metasurfaces: A Polarization Rotator Design. *Physical Review X*, **9**(1), 011,036, 2019.

[62] Z. Wu, C. Scarborough, A. Grbic. Space-Time-Modulated Metasurfaces with Spatial Discretization: Free-Space N-Path Systems. *Physical Review Applied*, **14**(6), 064,060, 2020.

[63] Y. Yamada. Dielectric Properties of Textile Materials: Analytical Approximations and Experimental Measurements—A Review. **2**(1), 50–80.

[64] F. Yang, D. T. Nguyen, B. O. Raeker, A. Grbic, J. S. Ho. Near-Reflectionless Wireless Transmission Into the Body With Cascaded Metasurfaces. *IEEE Transactions on Antennas and Propagation*, **70**(9), 8379–8388, 2022.

[65] F. Yang, B. O. Raeker, D. T. Nguyen, J. D. Miller, Z. Xiong, A. Grbic, J. S. Ho. Antireflection and Wavefront Manipulation with Cascaded Metasurfaces. *Physical Review Applied*, **14**(6), 064,044, 2020.

[66] Z. Yu, F. T. Alrashdan, W. Wang, M. Parker, X. Chen, F. Y. Chen, J. Woods, Z. Chen, J. T. Robinson, K. Yang. Magnetoelectric backscatter communication for millimeter-sized wireless biomedical implants. *Proceedings of the 28th Annual International Conference on Mobile Computing And Networking*, MobiCom '22, 432–445. Association for Computing Machinery, New York, NY, USA, 2022.

[67] R. I. Zelaya, R. Ma, W. Hu. Towards 6G and Beyond: Smarten Everything with Metamorphic Surfaces. *Proceedings of the Twentieth ACM Workshop on Hot Topics in Networks*, 155–162, 2021.

[68] R. I. Zelaya, W. Sussman, J. Gummeson, K. Jamieson, W. Hu. LAVA: fine-grained 3D indoor wireless coverage for small IoT devices. *Proceedings of the Conference of the ACM Special Interest Group on Data Communication (SIGCOMM)*, 123–136. ACM, 2021.

[69] P. Zhang, M. Rostami, P. Hu, D. Ganesan. Enabling Practical Backscatter Communication for On-body Sensors. *Proceedings of the 2016 ACM SIGCOMM Conference*, SIGCOMM '16, 370–383. Association for Computing Machinery, New York, NY, USA, 2016.